1
2
3 # Genetic Effects on Structural and Functional Properties of Sensorimotor-Association Axis of Cortical Organization are Selectively Distinct

4
5 Giacomo Bignardi[1,2*], Michel G. Nivard[3], H. Lina Schaare[4,5], Boris C. Bernhardt[6], Richard A.I.
6 Bethlehem[7,8], Simon E. Fisher[1,9,†], & Sofie L. Valk[4,5,10,† *]

7
8 [1] *Language and Genetics Department, Max Planck Institute for Psycholinguistics, Nijmegen, The*
9 *Netherlands;*
10 [2] *Max Planck School of Cognition, Leipzig, Germany;*
11 [3] *Department of Biological Psychology, Faculty of Behaviour and Movement Sciences, VU University,*
12 *Amsterdam, The Netherlands;*
13 [4] *Max Planck Institute for Human Cognitive and Brain Sciences, Leipzig, Germany;*
14 [5] *Research Center Jülich, Institute for Neuroscience and Medicine (INM-7), Germany;*
15 [6] *McGill University, Montreal, Canada;*
16 [7] *Autism Research Centre, Department of Psychiatry, University of Cambridge, Cambridge, United*
17 *Kingdom;*
18 [8] *Department of Psychology, University of Cambridge, Cambridge, United Kingdom;*
19 [9] *Donders Institute for Brain, Cognition and Behaviour, Radboud University, Nijmegen 6500 HB, The*
20 *Netherlands;*
21 [10] *Heinrich-Heine-Universitaet Duesseldorf, Germany*

22
23
24 * Giacomo Bignardi
25 * Sofie L Valk.
26 † These authors share last authorship.
27 **Email:** giacomo.bignardi@mpi.nl; valk@cbs.mpg.de

28
29

36

38
41 **This file includes:**
42   Main Text
43   Figures 1 to 5

Bignardi et al.

Abstract

The topological differentiation of sensorimotor and association cortical regions along a sensorimotor-association (S-A) axis has undergone profound evolutionary change along the mammalian lineage. In humans, patterns of gene expression, microstructure, and functional connectivity have been shown to vary systematically along such S-A axis. Despite robust spatial relationships between these different neurobiological traits, whether common genetic pressures shape the S-A axis across traits remains poorly understood. In this study, we exploit observed pervasive inter-individual variation in the S-A axis to capture its genetic architecture and to study shared common genetic sources of structure-function relationships. To do so, we applied a structural equation modeling framework, which reduced the issue of measurement error heterogeneity across the cortex and its impact on structure-function relationship estimates. We then used genetic relatedness across pairs of twins and removed intra-individual differences to focus on the reliable inter-individual differences along the S-A functional axis. Notwithstanding robust spatial relationships and highly heritable inter-individual differences in S-A axis microstructure and functional organisation, and contrary to group-level findings, our results indicate distinct genetic effects across the different S-A axis properties. Together, our observations challenge the notion of a common genetic cause for the association between S-A axis structural and functional properties. Our approach highlights the diversity of genetic origins of brain features that co-vary along the S-A axis, which is key to interrogating inter-individual variability in brain organisation and its consequences on cognition.

Bignardi et al.

Introduction

The human brain supports perception and action but also abstract cognition (1, 2). This diversity of functions is thought to be reflected by the gradual dissociation between unimodal sensory and transmodal association cortical areas along a sensorimotor-association (S-A) axis (3). The S-A axis spans a vast array of neuroanatomical properties, including microstructural variation (myelination and cytoarchitecture) and inter-areal connectivity distance (1, 3–6). Here, sensory areas show increased microstructural differentiation, myelination, and, predominantly, short-range connections. In contrast, association areas show less differentiated microstructural profiles, reduced myelination, and a combination of short- and long-range connectivity profiles (5, 7, 8). The S-A axis underwent profound evolutionary changes (3), with an expansion of cortical association areas paralleled by a marked laminarisation of sensory areas in human primates (9, 10). Such structural re-organisation and evolutionary changes along the S-A axis (1, 6, 11, 12) may have provided the scaffold for functional differentiation (13, 14), allowing in turn for human-specific cognitive and behavioural flexibility (1, 13).

In recent years, several discoveries have enhanced our understanding of the link between structural and functional features of the S-A axis. These findings have highlighted spatial associations between microarchitectonic differentiation (15) and cortical geometry (16) with intrinsic functional organisation (13, 17). For example, T1w/T2w maps derived from non-invasive Magnetic Resonance Imaging (MRI)—indexing cortical microstructural differences—have been shown to relate strongly to gene transcriptional profiles and functional dissociation along the S-A axis. This suggests that a canonical genetic architecture may shape S-A axis structural organisation, in turn allowing for the differentiation of cortical function (6). However, despite well-documented strong associations at the group-level (3, 4, 6, 18), it is still unclear whether common genetic pressure across different structural and functional features influences S-A axis variability between individuals. Therefore, here we asked whether common genetic effects are expected to shape structural and functional properties of the S-A axis similarly or whether, alternatively, genetic sources on S-A properties are distinct.

To answer our question, we first studied whether the S-A axis's structural and functional properties correlate. To do so, we shifted the focus of the analysis from the group to the individual level. First, we asked: do individual differences in structural properties of the S-A axis relate to differences in functional properties? In other words, we studied whether previously widely reported group averages can inform S-A axis associations at the individual level. Answering this question is a crucial step towards understanding the genetic architecture of the S-A axis, as individual differences can be further used as a window into the genetic basis of a trait (19). Specifically, we tested whether individual regional cortical microstructure (6) and structural cortico-cortical network proximity (20), captured by the geodesic distance of inter-connected regions across the cortical mantle (1, 20), relate to the well-known functional dissociations between sensory and transmodal association areas (1, 3). To account for the known issue of measurement error heterogeneity across the cortex (21) and its impact on association estimates (22), we applied and adapted measurement error models in the form of structural equation models (23, 24). This allowed us to tease apart unreliable intra-individual from reliable inter-individual variation in the

Bignardi et al.

121   functional organisation of the S-A axis. We then moved to answer our main question: Are genetic effects

122   on the S-A axis shared across structural and functional properties? Here, we analysed a genetic

123   informative sample and quantified the extent of overlap across genetic effects on structural and

124   functional properties of the S-A axis. Specifically, we used a twin-informed design to tease genetic

125   overlaps between the S-A axis's structural and functional properties. Last, we evaluated the robustness

126   of our results, both across subsamples, between regional and global cortical metrics, and between and

127   within individuals' S-A axis properties.

128

129   In summary, our study describes the specificity of genetic effects underlying the brain's different

130   structural and functional properties. This can inform further studies on the genetic origins of fundamental

131   principles of brain organisation and pave the way for research on the relationship between individual

132   variability in brain organisation principles and cognitive-behavioural differences.

133

134   **Results**

135   To quantify structural and functional S-A axis properties, we combined microstructural and resting-state

136   functional MRI (rsfMRI) data from the Human Connectome Project (HCP (25); N=992 adults; 529

137   women, mean age 28 y; 22-37 y). We computed two structural metrics and one functional metric

138   indexing the S-A axis:

139

140   • Regional microstructure: we quantified regional microstructure indexing the differentiation

141   between sensorimotor and association areas using the individuals' mean intensity of regional

142   T1w/T2w (T1w/T2w$_{mi}$) in 400 parcels (6, 26)

143   • Geodesic distance: we quantified regional cortico-cortical network proximity (20) by computing

144   the Geodesic Distance (GD) between every cortical region and its corresponding functional

145   network, averaging within each region to get parcel-wise estimates (27)

146   • Functional gradient loadings: we quantified individuals' functional S-A axis by obtaining the first

147   component of the individual functional connectomes (FC$_{G1}$) using diffusion map embedding (1)

148

149   We started our analysis by testing whether associations between group-level averaged maps of

150   structural S-A axis properties correlated with the functional S-A axis (Fig. 1A-C). By using a subsample

151   of n = 482 adults (229 women, mean age 28 y; 22-37 y; a subsample obtained by excluding respective

152   all twins included in the full HCP sample), we were able to replicate group-level findings between

153   averaged T1w/T2w$_{mi}$ and FC$_{G1}$, extending the results to GD and FC$_{G1}$ (Fig. 1D-E).

154

155   [Fig. 1 here]

156

157   **Pervasive inter-individual differences in the S-A axis of cortical organisation.** Having estimated

158   the extent of overlap between structural and functional S-A axis properties at the group-level, we shifted

159   the focus to the individual level. Since group-level S-A axis can mask substantial individual variability

160   (Fig. 2A), we asked: does individual variability in structural S-A axis properties relate to variability in S-

161 A functional properties, as for group-level analysis (Fig. 2B)? By shifting analysis from group-level

162 summary statistics to individual variability, we harnessed the fundamental distinction between intra- and

163 inter-individual differences (28). The first is known to index unreliable and fluctuating variability within

164 individuals over time, while the second indexes the reliable and stable part of the overall variability

165 between individuals (Fig. 2C) (28). This distinction is crucial, as intra-individual variability can downward

166 bias effect sizes, reduce statistical power (28), additionally downward biasing genetic estimates (29),

167 all of the above heterogeneously across the whole cortex (21), and can, therefore, increase

168 reproducibility issues (see (22) for details). We were able to make such a distinction by exploiting one

169 of the strengths of the HCP design, which emphasises multiple resting-state fMRI sessions (across two

170 days of scanning sessions, ~30 min each). This feature of the HCP design allowed us to discard

171 unreliable intra-individual fluctuations in rsfMRI data from reliable inter-individual differences in the

172 functional gradient. Precisely, we partition the inter-individual variance ($\sigma_{inter}^2 FC_{G1i}$) from the overall

173 observed variance in the functional gradient ($\sigma^2 FC_{G1i}$ for any parcel i) by applying a measurement error

174 model ((23, 24) Fig. 2D, see Methods).

175

176 Estimates obtained from the measurement error model indicate that 33% of the total variability in the

177 functional gradient was, on average, accounted for by intra-individual variance (Fig. 2E) even when

178 using individual functional gradients extracted from functional connectomes averaged across two days

179 of rsfMRI sessions (totalling ~60 min of scanning session). In other words, estimates for the association

180 between the functional gradient and other S-A axis properties (or any other variable) would be, on

181 average, biased downward by a factor of bias(r-observed, r-true) = 0.82 (a lower bound calculated

182 assuming perfect reliability for the other S-A axis property (22)). Second, we observed systematic

183 differences in estimates obtained from the measurement models across functional cortical networks,

184 $F(6, 393) = 33.21$, $p < .001$; $\eta^2 = 0.34$, 95% CI [0.27, 1.00]), with estimates for parcel-wise inter-individual

185 variances ranging from $\sigma_{inter-114}^2 = .39$ to $\sigma_{inter-294}^2 = .89$ (Figure 2D, SI Appendix, Fig. S1). In other

186 words, bias is heterogeneous and expected to influence estimates across the cortex systematically.

187

188   [Fig. 2 here]

189

190 **Individual differences in regional cortico-cortical network proximity, rather than microstructure,**

191 **relate to the functional gradient of the S-A axis of cortical organisation.** To simultaneously de-

192 attenuate the heterogenous downward biases and handle structural and functional S-A metrics, we

193 used a Structural Equation Modeling (SEM) approach. Precisely, we specified a model in which the

194 inter-individual differences in the functional gradient estimated via the measurement error model were

195 directly tested for associations with microstructural profiles and geodesic distances parcel-wise data

196 (Fig. 3A). Here, we note that we avoided making assumptions about the causal structure generating

197 the possible correlations between structural and functional metrics. We simply limited ourselves to

198 estimating the association between regional properties of the S-A axis. On the one end, conversely to

199 group-level topographies, we found less than 2% of the 400 parcels to display a significant association

200 between individuals' microstructural profiles and functional gradient loadings (Fig. 3B). These significant

201 associations were all negative, weak (-.20 > r > -.27), and spread across both hemispheres and the

202 dorsal, ventral, and default-mode functional networks. Conversely, we found large overlaps between

203 individual geodesic distances and functional gradient loadings (Fig. 3C), with 57% of the 400 parcels

204 showing significant associations after Bonferroni correction. The directionality of the estimates for the

205 association between individual regional geodesic distances and functional gradient loadings highlighted

206 systematic differences across functional networks. Significant positive associations were preferentially

207 clustered within the visual and the default mode (one sample t-test, two-sided, $t(21)$ = 5.82, p < .001,

208 average r = .51, and $t(53)$ = 4.04, p = .001, average r = .25), while negative associations where

209 preferentially clustered within the somatomotor and ventral attention networks (one sample t-test, two-

210 sided, $t(59)$ = -13.32, p < .001, average r = -.48, and $t(27)$ = -8.14, p < .001, average r = -.40,

211 respectively, all test corrected for Bonferroni). Estimates obtained from standard correlation analysis

212 further confirmed that the SEM approach successfully de-attenuated measurement error bias (SI

213 Appendix, Fig. S2).

214

215 [Fig. 3 here]

216

217 **Genetic effects on regional S-A axis variability are substantial yet mostly distinct.** After having

218 related inter-individual differences in structural and functional S-A axis properties, we asked whether

219 genetic effects were mostly common or distinct across S-A axis properties. Here, we further exploited

220 the HCP's family structure to partition the relationship between structural and functional properties of

221 the S-A axis in common and distinct genetic sources. Precisely, by applying a multivariate twin design,

222 we were able to partition genetic (σ^2_A; A: additive) and unsystematic environmental (σ^2_E; E: Unique-

223 Environmental) sources of variability in microstructure, geodesic distances, and functional gradients

224 loadings. (Here, we note that since intra-individual variability is partitioned in the E component of the

225 model (30), this strategy made it also possible to discard further intra-individual sources of variance in

226 structural metrics, even in the absence of repeated measures (29)). To do so, we focused our analysis

227 on the twin HCP subsample, which includes both monozygotic (MZ) and dizygotic (DZ) twins (n = 328,

228 195 MZ and 133 DZ individual twins, 124 and 88 women, respectively; mean age 29 y, range=22-35 y;

229 see Methods for details on inclusion criteria).

230

231 To partition sample variability (σ^2_p; p: S-A axis phenotypic property) within S-A modalities in σ^2_A and σ^2_E

232 sources and further unpack genetic and environmental structure-function associations, we specified a

233 multigroup multivariate model with only A and E components (Fig. 4A). Microstructural profiles,

234 geodesic distances, and functional gradients loadings all displayed substantial heritability (h^2_{twin}), with

235 mean h^2_{twin} =.43, sd =.11, mean h^2_{twin} =.34, sd =.11, and mean h^2_{twin} =.57, sd =.14, respectively.

236 Consistent with previous work (24), a comparison of univariate models fitted to functional gradient

237 loadings not accounting for measurement error confirmed that the inclusion of the measurement error

238 model substantially boosted h^2_{twin} estimates of 54% relative to h^2_{twin} not accounting for intra-individual

239 variance (univariate h^2_{twin} = .37, sd =.11 when not including a measurement error model, see SI

240 Appendix, Fig. S3). However, notwithstanding such relatively high h^2_{twin} for both microstructural profiles

241 and functional gradient loadings, we found no significant additive genetic correlation between the two

242 (all p > .05, Bonferroni corrected; Fig. 4B). This suggested little room for possible common genetic

243 causes between microstructural intensity and functional gradient loadings S-A axis properties.

244 Conversely, 14% of the parcels displayed significant additive genetic correlations between geodesic

245 distances and functional gradient loadings (7% negative and 6% positive in directionality, respectively

246 p < .05, Bonferroni corrected, Fig. 4C). The average magnitude of the genetic correlation (r_A) was r_A =

247 -0.67, sd = .16, and r_A = .64, sd = .16, for the negative and positive association, respectively.

248 Furthermore, we found that for 30% of the parcels, complementary environmental effects mostly

249 correlated between geodesic distances and functional gradient loadings.

250

251   [Fig. 4 here]

252

253 **Associations between structural and functional properties of the S-A axis are robust across**

254 **samples.** To test for the robustness of the results discussed so far, we estimated the overlap of the

255 significant regional genetic or environmental association in the genetically informative subsample with

256 the significant regional associations obtained from the first subsample. Of the 104 parcels that displayed

257 either or both significant genetic and environmental correlations between geodesic distances and

258 functional gradient loadings in the genetically informative sample, 99 also displayed a significant

259 correlation in the first subsample. In other words, we found a 95% overlap between subsamples. These

260 results show that regional results were robust across two subsamples drawn from the HCP.

261

262 **Genetic and environmental associations extend beyond regional S-A axis variability.** As a final

263 analysis, we asked whether associations between geodesic distances and functional gradients were

264 generalisable beyond regional differences. First, we quantified global S-A axis properties variability as

265 the overall Median Absolute Deviation (MAD) across all parcels within individuals. Within an individual,

266 higher MAD scores indicate a larger dispersion in S-A axis values across the cortex. Once more, we

267 found no significant genetic or environmental associations between microstructural profile intensity and

268 functional gradients. Yet, we found a substantial negative genetic correlation between the geodesic

269 distances and functional gradient between individuals' S-A axis MAD scores (r_A = -.78, 95% CI [-1.19,

270 -.34], CFI = .93, RMSEA = 0.04; Fig. 5A). Additionally, to get a complementary estimate of global S-A

271 axis variability, we quantified microstructural profile intensity, geodesic distance, and functional gradient

272 ρ similarity indices. These indices assessed how similar S-A axis properties in one individual are

273 compared to the average. Consistent with regional and global variances differences, ρ similarity indices

274 in geodesic distance, rather than microstructure, showed strong and positive genetic correlations with

275 global differences in the functional gradient (r_A = .61, 95% CI [.43, .79], CFI = .95, RMSEA = 0.04; Fig.

276 5B). Findings were robust to ICV as a possible common cause of S-A axis structure-function covariance

277 (SI Appendix, Fig. S4)

278

279   [Fig. 5 here]

280

Discussion

281 Notwithstanding the relatively high heritability of the S-A axis properties as shown in this study,
282 theoretical models of S-A axis development and evolution (3), and group-level relationships between
283 patterns of gene expression, cortical microstructure, and functional differentiation of sensorimotor to
284 transmodal-association areas (6), we found little evidence for shared genetic effects between
285 microstructural and functional S-A axis similarities. Precisely, we found little evidence of phenotypic and
286 an absence of evidence for genetic or environmental associations between cortical microstructure (as
287 measured by T1w/T2w) and S-A function (as measured by the principal gradient of functional
288 connectivity) of the cortex. These results, which accounted for measurement error and held across
289 regional and global cortical metrics and between and within individuals, do not support the hypothesis
290 of substantial common genetic pressure on S-A axis microstructural and functional similarities.

291 At the same time, our results showed substantial genetic and environmental associations between
292 individual-level differences in regional and global cortico-cortical network proximity (as measured by the
293 geodesic distance of inter-connected regions across the cortical mantle) and function. These latter
294 results align with theories emphasising geometric constraints of brain function yet do not fully align with
295 previous and current group-level estimates. While group-level associations indicate a positive
296 relationship between cortico-cortical network proximity, our results indicate a mixture of positive and
297 negative relationships at the individual level of analysis (the former preferentially clustered within the
298 visual and default mode network, the latter with the somatomotor and the ventral attention network).
299 Moreover, we found negative, not positive, genetic correlations when shifting from local to global
300 association, as we did when analysing overall within-individual S-A axis dispersion. This suggests that
301 genetic differences between people that tend to co-occur with decreased variation in geodesic distances
302 across the cortex also tend to co-occur with more dispersed functional gradients. These results, in line
303 with the results obtained by analysing microstructural differences between individuals, collectively
304 reveal that group-level estimates, such as the ones previously reported in the literature, might mask
305 pervasive inter-individual differences. These inter-individual differences, in turn, might display different
306 patterns of associations to the one depicted at the group level.

310 Based on group-level associations, previous work suggested that cortical maturation of diverse
311 neurobiological properties proceeds along a conformed evolutionarily and developmentally rooted S-A
312 axis of cortical organisation (3, 4). However, our results indicate that genetic variants within a population
313 are selectively associated with some properties (e.g., function and cortico-cortical network proximity)
314 but not others (e.g., microstructure). This selective distinctness of the genetic correlates of structural
315 and functional properties of the S-A axis might indicate that common genetic pressures influencing the
316 development of the S-A axis across cortical properties reached fixation in the population and, therefore,
317 are not detectable using analysis at the level of the individuals. Another possible explanation for our
318 results may lie in the physiological and cognitive implication of the resting state signal and downstream
319 effects on its functional gradient. It is possible that, although generally resting state networks are
320 topologically organised along the S-A axes, their individual fluctuations reflect physiological variability

321 not captured by its microstructural scaffold (31). Indeed, various works have reported network
322 integration and segregation to align with neural gain, which could be explained by alterations in
323 neuromodulatory systems (32, 33).

324

325 While these findings may provide little information on the shared genetic pressure that gives rise to the
326 development of the S-A axis at the group level, they could be particularly relevant for studies on the
327 origin of differences between individuals, such as in various neuropsychiatric disorders or work on brain-
328 behaviour associations in general. For example, recent studies noted a compression of the S-A
329 functional axis in individuals with autism (27), schizophrenia (34), and depression (35), highlighting an
330 association between atypical cortical functional segregation and psychiatric conditions. Complementing
331 the latter studies with informative genetic models of structural and functional S-A axis variability would
332 allow us to see whether and which genetic effects on S-A variability might partially explain psychiatric
333 conditions, facilitating mechanistic insights in notoriously complex phenotypes. We also note that these
334 models can be easily applied to many neurobiological properties (e.g., resting-state fMRI, see (24)) to
335 enhance current brain-behaviour mapping efforts (36). To facilitate such endeavours, we have made
336 all the code available and provided all SEM functions in R and lavaan syntax to apply multivariate twin
337 and measurement error modelling.

338

339 The measurement error modeling approach can successfully tease apart unstable intra-individual
340 differences from stable inter-individual differences, and this effect can have a substantial downstream
341 impact on estimates. For example, applying the measurement error modeling approach, in line with
342 previous results, resulted in a nearly 1.5-fold increase in heritability. We foresee that this approach
343 could have further direct application in the undergoing research on the origins of psychiatric disorders
344 and brain-behaviour studies and in the analysis of the genomic architecture of principles of brain
345 organisation, for example, by mitigating the impact of measurement error heterogeneity on estimates.
346 Indeed, when individual variability in the S-A axis is the predictor of interest, such as in brain-behaviour
347 studies, applying any measurement error model is expected to deattenuate downwardly biased
348 estimates (22, 28, 37, 38). Moreover, genome-wide association studies could easily implement
349 genome-wide or genomic structural equation modeling (39, 40) extension of our approach to discard
350 unstable and unreliable variance, overcoming attenuation biases in single nucleotide polymorphism to
351 phenotype association (e.g., similarly to what has been done for polygenic indices based analyses (38)).
352 However, even when these tools are applied to overcome attenuation biases in brain-behaviour
353 association studies, associations should still be expected to be small (36). Therefore, caution should
354 still be applied when designing a study.

355

356 It is worth noting that our study comes with the limitation of an absence of repeated measures for
357 structural metrics. Although applying a measurement error model allowed us to disentangle intra- to
358 inter-individual variability in functional gradient loadings, we could not account for the differences in
359 structural properties within individuals. This limitation may have attenuated the estimated relationship
360 between structure and function. However, the nature of the metrics and the twin design employed to

361   elucidate differences between individuals should mitigate the impact of such a lack of repeated
362   structural metrics (29). By applying the classical twin design, we were able to further partition unstable
363   measurement error in the environmental (E) component of the model, which minimised any possible
364   bias introduced by hypothetical measurement error, at least for the additive genetic (A) correlations (r_A)
365   estimates.

366

367   In sum, our findings reveal that group-level results can overshadow substantial inter-individual
368   differences within and between different neurobiological properties. Focusing on these previously
369   underappreciated differences, we could highlight selective associations of individual variation in S-A
370   axis cortical structure and function. These inter-individual differences and associations open a window
371   into genetic sources of S-A axis structure and function, which we reveal to be selectively distinct. These
372   results underscore the complex interplay between the S-A axis's structural and intrinsic functional
373   properties, providing the readers with a set of tools that can be used to test their potential differential
374   roles in shaping cognition.

375

376   **Materials and Methods**
377   **Sample.** We used data from the Human Connectome Project (HCP) S1200 release. The HCP includes
378   data from 1206 individuals (656 women) that comprise 298 Monozygotic (MZ) twins, 188 Dizygotic (DZ)
379   twins, and 720 singletons, with mean age ± *sd* = 28.8 ± 3.7 years (age range = 22-37 years). Informed
380   consent for all individuals was obtained by HCP, and our data usage was approved by HCP and
381   complied with all relevant ethical regulations for working with human participants (see (13, 25, 41)). The
382   primary participant pool comes from individuals born in Missouri to families that include twins, sampled
383   as healthy representatives of ethnic and socioeconomic diversity of US individuals, based on data from
384   the Missouri Department of Health and Senior Services Bureau of Vital Records. We followed standard
385   guidelines for inclusion criteria as described elsewhere (13). Our sample, in line with Valk et al., (13)
386   comprised 992 (529 women) individuals. The first subsample of *n* = 482 (229 women) was created by
387   excluding all individual twins. The second genetically informative subsample of *n* = 328 (212 women)
388   was created by including only individual twins with genotyped zygosity matching self-reported zygosity
389   (195 MZ and 133 DZ; 124 women and 88 women, respectively).

390

391   **Functional imaging.** Functional connectivity matrices were based on four 14 min 33 s of functional
392   Magnetic Resonance Imaging (fMRI) data acquired over two sessions, spaced two days apart, through
393   the HCP, which underwent HCP's minimal preprocessing. For each individual, four functional
394   connectivity matrices were computed using the minimally preprocessed, spatially normalised resting-
395   state fMRI (rsfMRI) scans, which were co-registered using MSMAll to template HCP 32k_LR surface
396   space. 32k_LR surface space consists of 32,492 total nodes per hemisphere (59,412 excluding the
397   medial wall). We computed four functional connectivity matrices per individual from the average time
398   series extracted in each of the 400 Schaefer cortical parcels. The individual functional connectomes
399   were generated by averaging preprocessed time series within nodes, Pearson correlating nodal time

400 series and converting them to Fisher-z scores. The average functional connectomes were obtained by
401 averaging functional connectomes within individuals (i.e., between sessions) and between individuals.

402 **Structural imaging.** MRI protocols of the HCP have been previously described (25, 41). MRI data were
403 acquired originally on the same day on the HCP's custom 3T Siemens Skyra equipped with a 32-
404 channel head coil. T1w images with identical parameters were acquired using a 3D-MP-RAGE
405 sequence over 7 min 40 s (0.7 mm isovoxels, matrix = 320 × 320, 256 sagittal slices; TR = 2400 ms,
406 TE = 2.14 ms, TI = 1000 ms, flip angle = 8°; iPAT = 2). T2w images were acquired using a 3D T2-
407 SPACE sequence with identical geometry over 8 min and 24 s (TR = 3200 ms, TE = 565 ms, variable
408 flip angle; iPAT = 2). We followed the preprocessing steps outlined in Valk et al. (13).

409 **Parcellation and functional networks**. We used the Schaefer group-level hard-parcellation, originally
410 obtained by a gradient-weighted Markov random field model integrating local gradient and global
411 similarity approaches (26). To stratify results within established cortical functionally coupled networks,
412 we used the seven Yeo-Krienen networks (42).

413 **Microstructural profiles (T1w/T2w$_{mi}$).** We used T1w/T2w imaging myelin-sensitive contrast from the
414 HCP minimal processing pipeline, which uses the T2w to correct for inhomogeneities in the T1w image
415 to estimate mean intensity T1w/T2w microstructural profiles (T1w/T2w$_{mi}$). T1w/T2w$_{mi}$ has been shown
416 to map to model-based tract-tracing histological data in macaque, estimate intracortical myelin content,
417 and thus approximate architectural complexity and cortical hierarchy (6).

418 **Geodesic distance (GD).** Individual Geodesic Distances (GD) were computed using the Micapipe
419 toolbox (20). Briefly, we computed GD between each region and their top 10% of maximally functionally
420 connected regions along each individual native cortical midsurface. We further averaged within regions
421 to obtain a parcel-wise value and improve computation performance. Micapipe implements the Dijkstra
422 algorithm (43) (further details can be found in (20)).

423 **Functional gradient loadings (FC$_{G1}$).** We sequentially averaged FCs, first within days, resulting in two
424 FCs per individual, and then between days, resulting in one FC per individual. We then extracted the
425 three first components from the two sequentially averaged and one averaged FCs, using the Python
426 package BrainSpace (44). Extraction of the first eigenvector followed standard procedures, with the
427 original individual FCs set at a connection density of 10% (i.e., the FCs were made sparse by setting a
428 sparsity threshold of 90%). The first ten eigenvectors were then obtained by decomposing the FCs by
429 diffusion map embedding, a robust non-linear manifold learning technique (1). To aid comparability
430 across individuals, we aligned individual eigenvectors to the template eigenvector by Procrustes
431 rotation (45). The template functional gradient was directly extracted from the overall mean FC matrix.

432 **Group-level associations analysis.** We computed Spearman rank-order correlations (ρ) between the
433 structural (T1w/T2w$_{mi}$ and GD) and functional (FC$_{G1}$) S-A axis group-level properties. Group-level
434 properties were obtained from the average of the individual structural S-A properties (i.e., average
435 T1w/T2w$_{mi}$ and GD), and from the decomposition of the average FC (i.e., principal gradient obtained
436 via diffusion map embedding of the average FC).

437 **Measurement model of error in individual variability of the functional S-A axis.** To partition stable
438 inter-individual variability in functional gradient loading, we adapted previous measurement error
439 models to rsfMRI to gradients (23, 24). The intuition behind such a modeling strategy is simple. Suppose
440 parcel-wise values are measured without error and are stable over a reasonable period of time (e.g.,
441 one day). In that case, the correlations across individuals between the values obtained across two time
442 points will equal 1. If the correlations deviate from 1 instead, regional values will be measured with
443 some error, with bigger deviations corresponding to higher error or fluctuation over time. When errors,
444 or changes over time, are present, we can use the measurement error model to estimate what stays
445 constant across time, indexing the "true" regional values. Across the manuscript, for correctness, since
446 "error" variance can include meaningful, yet unstable, fluctuation in rsfMRI, while "true" variance can
447 also consist of systematic measurement error across sessions, we refer to the former term as intra-
448 individual and the latter as inter-individual variability (28). First, we fit a measurement model to parcel-
449 wise functional gradient loadings averaged within days. In line with Teeuw et al. (24), we did not
450 constrain intra-individual variance components to be equal across days of scanning sessions. We
451 performed model fitting in lavaan (44) after standardising observed variables (i.e., std.ov = T). We then
452 used model estimates obtained for the variances of the latent and observed components. Using
453 Spearman-Brown correction, we computed the averaged proportion of stable inter-individual variance
454 in functional gradient loadings across days as the intra-class correlation (ICC) (46). For each parcel *i,*
455 the ICC was calculated as follows:

456
$$\text{ICC}(2, k)_{(i)} = \frac{k * \text{ICC}(2,1)_{(i)}}{1 + (k - 1) * \text{ICC}(2,1)_{(i)}}$$

457 Where *k* is a constant equal to the number of measures (i.e., *k* = 2) and the $\text{ICC}(2,1)_{(i)}$ is calculated as
458 follows:

459
$$\text{ICC}(2,1)_{(i)} = \frac{\sigma^2_{\text{inter}(i)}}{\sigma^2_{\text{inter}(i)} + (\frac{\sigma^2_{1-\text{intra}(i)} + \sigma^2_{2-\text{intra}(i)}}{2})}$$

460 $\text{ICC}(2,k)_{(i)}$ estimates the proportion of inter-individual variance over the total variance, $\sigma^2_{\text{inter}(i)}$, in the
461 functional loadings as if they were obtained from the average of the two scanning sessions. The
462 proportion of intra-individual variance for a parcel *i*, $\sigma^2_{\text{intra}(i)}$, is obtained simply by subtracting the
463 $\text{ICC}(2,k)_{(i)}$ from 1.

464 The expected bias for any parcel *i* was calculated following Tiego et al. (22):

465
$$\text{bias}_{(i)} = \sqrt{R_{\text{p,p}} * R_{\text{FCG1,FCG1}(i)}}$$

466 Where $R_{\text{p,p}}$, the reliability for the structural S-A axis property *p* (e.g., T1w/T2w$_{\text{mi}}$), was set to be equal
467 to 1 across all parcels, and $R_{\text{FCG1,FCG1}(i)}$, the reliability of parcel-wise value for the functional gradient
468 loading, was calculated as $\text{ICC}(2,k)_{(i)}$.

Bignardi et al.

469 **Structural Measurement Error Equation Modeling.** We used Structural Equation Modeling (SEM) to
470 estimate correlations between structural (i.e., $T1w/T2w_{mi(i)}$, $GD_{(i)}$) and functional (i.e, $FC_{G1(i)}$) S-A
471 modalities. Each multivariate model simultaneously accounted for intra-individual variances by including
472 the measurement error model. All models were fitted in lavaan (47) after standardising all observed
473 variables (i.e., std.ov = T). Prior to model fitting, sex and age were regressed from parcel-wise S-A axis
474 values using the function umx::umx_residualize() (48). Structural equation models were fit to residual
475 scores. We assumed missing data to be missed at random and followed parameters' estimation via full-
476 information Maximum Likelihood (i.e., missing = "ML").

477 **Twin-informed Multivariate Structural Equation Modeling.** We used multigroup SEM to partition
478 parcel-wise variability in structural ($\sigma^2 T1w/T2w_{mi(i)}$, $\sigma^2 GD_{(i)}$) and functional ($\sigma_{inter}^2{}_{(i)}$) S-A modalities into
479 either additive genetic (σ^2_A) and unsystematic environmental (σ^2_E) sources of variance. Structural
480 equation models were fit to $T1w/T2w_{mii}$, GD_i, and FC_{G1i1} (day 1) and FC_{G1i2} (day 2) data, grouped by
481 zygosity (i.e., two groups). The model specification was informed by the multivariate twin design (49).
482 Briefly, monozygotic (MZ) twins are ~100 % genetically identical, coming from the same fertilised egg.
483 In contrast, dizygotic (DZ) twins are, on average, only 50% additively genetically similar regarding allelic
484 variants coming from two different fertilised eggs. Thus, the correlation between the additive genetic
485 component (A) is set to be equal to 1 for MZ while .5 for DZ. In contrast, each twin's unique environment
486 (E) component will be unique; therefore, their correlation will be equal to 0. In total, we fit one
487 multivariate AE model per parcel. Following the measurement error procedure outlined above and (24),
488 a common pathway measurement error model was included in the specification of the multigroup SEM.
489 As such, each multivariate model simultaneously accounted for intra-individual variance. We employed
490 the direct symmetric approach by estimating variance components directly while setting path
491 coefficients to 1 (with the exception of the measurement model, for which we fixed the variance to be
492 equal to 1, and estimated the path coefficients, instead). We chose this approach as it has been shown
493 to reduce type I errors and produce asymptotically unbiased χ^2 (50).

494 All models were fitted in lavaan (47), with standardisation of observed variables before model fitting
495 (i.e., std.ov = T). Similarly to what was reported above, to control for the effect of age and sex on S-A
496 axis properties, we residualised parcel-wise variables prior to modeling using the function
497 umx::umx_residualize() (48). Residuals were used as observed variables in later twin modeling. We
498 estimated parameters via full-information Maximum Likelihood (i.e., missing = "ML") and evaluated the
499 goodness of fit for each parcel by comparative fit index (CFI) and root mean square error of
500 approximation (RMSEA) scores. Following standard cut-offs (24), we retained only models with a
501 "satisfactory" CFI>.90 and an RMSEA<.08. Narrow-sense twin heritability (h^2_{twin}) estimates for each
502 parcel *i* were defined as the ratio of the additive genetic variance over the sum of the additive genetic
503 and environmental variances:

504
$$h^2_{\text{twin-p(i)}} = \frac{\sigma^2_{Ap(i)}}{\sigma^2_{Ap(i)} + \sigma^2_{Ep(i)}}$$

505 Where $\sigma^2_{Ap(i)}$ is the additive genetic variance for the S-A axis parcel-wise value for the given property p

506 (e.g., GD). For functional gradient loadings, the heritability was calculated as

507
$$h^2_{\text{twin-inter(i)}} = \sigma^2_{\text{Ainter(i)}}$$

508 After imposing the equality constrain on the common factor $FC_{\text{G1}inter(i)}$

509
$$\sigma^2_{\text{Ainter(i)}} + \sigma^2_{\text{Einter(i)}} = 1$$

510 Genetic correlations (r_A) were calculated as:

511
$$r_A = \frac{\sigma_{\text{Ap1i,Ap2i}}}{\sqrt{\sigma^2_{\text{Ap1i}} * \sigma^2_{\text{Ap2i}}}}$$

512 Where $\sigma_{Ap,Ap2}$ is the additive genetic covariance between two S-A axis property $p1$ and $p2$ (e.g., GD

513 and T1w/T2w$_{\text{mi}}$). Environmental correlations were calculated similarly to r_A but using environmental

514 variance and covariances estimates.

515 **Generalisation beyond regional associations.** For each individual, we obtain two metrics for

516 structural and functional S-A axis properties (i.e., a total of six measures per individual) :

517 *Overall within-individual Median Absolute Deviation*: we quantified the spread of the regional values

518 across the cortex by computing within-individual Median Absolute Deviation (MAD) of microstructure,

519 geodesic distances, and functional gradient loadings. MAD is a robust univariate measure of statistical

520 dispersion and is simply calculated as follows:

521
$$MAD_{pj} = med(|p_{pji} - med(p_{pj})|)$$

522 Where p$_{ij}$ is the parcel-wise value for a property p, an individual j, and a parcel I and *med* is the median.

523 *ρ similarity index*: we obtained the similarity index by estimating the Spearman rank (ρ) correlations

524 between each individual microstructure, cortico-cortical network proximity, and functional gradient

525 loadings with the respective S-A group-level modality vectors. For example, the ρ similarity index for the

526 cortico-cortical network proximity for an individual j was obtained by correlating their GD with the group-

527 level GD. Similarly, for the same individual j, the similarity index for their functional gradient loading was

528 obtained by correlating their FC_{G1} on day 1 and on day 2 of scanning with the group-level FC_{G1}.

529 Similar to what is outlined above for regional analysis, we fit two multivariate AE models, one per metric.

530 Before model fitting, ρ similarity indices were first Fisher-z transformed. To recapitulate regional analysis

531 as closely as possible within the multivariate model, we also included the measurement error model to

532 overall within-individual MAD and ρ similarity index functional gradient loadings obtained on days 1 and

533 2 of scanning sessions. Note that standardised coefficients are obtained using the

534 lavaan::standardizedSolution() function. As a final sensitivity analysis, to discount individuals' whole

535 brain volume as a possible confounding effect of the relationship between SA axis structure-function

536 associations, we additionally included total Intra-Cranial volume (ICV). Precisely, we followed a two-

Bignardi et al.

537   step procedure to discount ICV as a possible common cause. First, we regressed out ICV from overall

538   within-individual MAD and Fisher-z transformed ρ similarity indices for all S-A axis properties. We then

539   re-fit the exact multivariate twin models to the residuals.

540

541   **Data availability**

542   We obtained human data from the open-access Human Connectome Project (HCP) S1200 young

543   adult sample. HCP Young Adult data are available at https://www.humanconnectome.org/study/hcp-

544   young-adult. Supporting Files 1-5 with summary statistics can be found at

545   https://github.com/giacomobignardi/h2_SA_axis/tree/main/SI.

546

547   **Code availability**

548   All code is available and can be found at https://github.com/giacomobignardi/h2_SA_axis . SEM and

549   twin-based analysis have been done using the statistical package latent variable analysis (lavaan)

550   https://lavaan.ugent.be/. The function to apply the measurement error model (meermo) can be found

551   here https://github.com/giacomobignardi/h2_SA_axis/tree/main/R/functions/meermo. lavaan syntax for

552   latent variable analysis of twin data (lavaantwda) can be found following the repository

553   https://github.com/giacomobignardi/h2_SA_axis/tree/main/R/functions/lavaantwda. An introduction to

554   twin modeling using lavaan can be found at https://rpubs.com/MichelNivard/798608. Code and tutorial

555   for functional gradient decomposition of functional connectomes are available

556   at https://brainspace.readthedocs.io/en/latest/pages/install.html. The code and tutorial to generate

557   geodesic distances can be found at https://micapipe.readthedocs.io/en/latest/.

558

568 **References**

569   1.   D. S. Margulies, *et al.*, Situating the default-mode network along a principal gradient of
570   macroscale cortical organization. *Proc. Natl. Acad. Sci.* **113**, 12574–12579 (2016).

571   2.   M. M. Mesulam, From sensation to cognition. *Brain* **121**, 1013–1052 (1998).

572   3.   V. J. Sydnor, *et al.*, Neurodevelopment of the association cortices: Patterns, mechanisms, and
573   implications for psychopathology. *Neuron* **109**, 2820–2846 (2021).

574   4.   V. J. Sydnor, *et al.*, Intrinsic activity development unfolds along a sensorimotor–association
575   cortical axis in youth. *Nat. Neurosci.* **26**, 638–649 (2023).

576   5.   C. F. von Economo, G. N. Koskinas, Die cytoarchitektonik der hirnrinde des erwachsenen
577   menschen. *J Springer* (1925).

578   6.   J. B. Burt, *et al.*, Hierarchy of transcriptomic specialization across human cortex captured by
579   structural neuroimaging topography. *Nat. Neurosci.* **21**, 1251–1259 (2018).

580   7.   K. Brodmann, ergleichende Lokalisationslehre der Grosshirnrinde in ihren Prinzipien dargestellt
581   auf Grund des Zellenbaues. *Barth* (1909).

582   8.   M. Ercsey-Ravasz, *et al.*, A predictive network model of cerebral cortical connectivity based on a
583   distance rule. *Neuron* **80**, 184–197 (2013).

584   9.   R. L. Buckner, F. M. Krienen, The evolution of distributed association networks in the human
585   brain. *Trends Cogn. Sci.* **17**, 648–665 (2013).

586   10.   M. Á. García-Cabezas, J. L. Hacker, B. Zikopoulos, Homology of neocortical areas in rats and
587   primates based on cortical type analysis: an update of the Hypothesis on the Dual Origin of the
588   Neocortex. *Brain Struct. Funct.* **228**, 1069–1093 (2023).

589   11.   A. Saberi, *et al.*, The regional variation of laminar thickness in the human isocortex is related to
590   cortical hierarchy and interregional connectivity. *PLoS Biol.* **21**, e3002365 (2023).

591   12.   N. T. Markov, *et al.*, Cortical high-density counterstream architectures. *Science* **342**, 1238406
592   (2013).

593   13.   S. L. Valk, *et al.*, Genetic and phylogenetic uncoupling of structure and function in human
594   transmodal cortex. *Nat. Commun.* **13**, 2341 (2022).

595   14.   M. Demirtaş, *et al.*, Hierarchical Heterogeneity across Human Cortex Shapes Large-Scale Neural
596   Dynamics. *Neuron* **101**, 1181-1194.e13 (2019).

597   15.   C. Paquola, K. Amunts, A. Evans, J. Smallwood, B. Bernhardt, Closing the mechanistic gap: the
598   value of microarchitecture in understanding cognitive networks. *Trends Cogn. Sci.* **26**, 873–886
599   (2022).

600   16.   R. Leech, *et al.*, Variation in spatial dependencies across the cortical mantle discriminates the
601   functional behaviour of primary and association cortex. *Nat. Commun.* **14**, 5656 (2023).

602   17.   L. E. Suárez, R. D. Markello, R. F. Betzel, B. Misic, Linking Structure and Function in Macroscale
603   Brain Networks. *Trends Cogn. Sci.* **24**, 302–315 (2020).

604   18.   J. M. Huntenburg, P.-L. Bazin, D. S. Margulies, Large-Scale Gradients in Human Cortical
605   Organization. *Trends Cogn. Sci.* **22**, 21–31 (2018).

606   19.   E. A. Willoughby, T. J. C. Polderman, B. B. Boutwell, Behavioural genetics methods. *Nat. Rev.*
607   *Methods Primer* **3**, 1–16 (2023).

608 20. R. R. Cruces, *et al.*, Micapipe: A pipeline for multimodal neuroimaging and connectome analysis.
609   *NeuroImage* **263**, 119612 (2022).

610 21. K. Helwegen, I. Libedinsky, M. P. van den Heuvel, Statistical power in network neuroscience.
611   *Trends Cogn. Sci.* **27**, 282–301 (2023).

612 22. J. Tiego, *et al.*, Precision behavioral phenotyping as a strategy for uncovering the biological
613   correlates of psychopathology. *Nat. Ment. Health* **1**, 304–315 (2023).

614 23. A. M. Brandmaier, *et al.*, Assessing reliability in neuroimaging research through intra-class effect
615   decomposition (ICED). *eLife* **7**, e35718 (2018).

616 24. J. Teeuw, H. E. Hulshoff Pol, D. I. Boomsma, R. M. Brouwer, Reliability modelling of resting-state
617   functional connectivity. *NeuroImage* **231**, 117842 (2021).

618 25. D. C. Van Essen, *et al.*, The Human Connectome Project: A data acquisition perspective.
619   *NeuroImage* **62**, 2222–2231 (2012).

620 26. A. Schaefer, *et al.*, Local-Global Parcellation of the Human Cerebral Cortex from Intrinsic
621   Functional Connectivity MRI. *Cereb. Cortex* **28**, 3095–3114 (2018).

622 27. S.-J. Hong, *et al.*, Atypical functional connectome hierarchy in autism. *Nat. Commun.* **10**, 1022
623   (2019).

624 28. X.-N. Zuo, T. Xu, M. P. Milham, Harnessing reliability for neuroscience research. *Nat. Hum.*
625   *Behav.* **3**, 768–771 (2019).

626 29. F. A. Hagenbeek, *et al.*, Maximizing the value of twin studies in health and behaviour. *Nat. Hum.*
627   *Behav.* **7**, 849–860 (2023).

628 30. D. S. Falconer, T. F. C. Mackay, *Introduction to Quantitative Genetics*, 4 edition (Pearson, 1996).

629 31. T. O. Laumann, A. Z. Snyder, Brain activity is not only for thinking. *Curr. Opin. Behav. Sci.* **40**,
630   130–136 (2021).

631 32. J. M. Shine, M. J. Aburn, M. Breakspear, R. A. Poldrack, The modulation of neural gain facilitates
632   a transition between functional segregation and integration in the brain. *eLife* **7**, e31130 (2018).

633 33. A. I. Luppi, *et al.*, In vivo mapping of pharmacologically induced functional reorganization onto the
634   human brain's neurotransmitter landscape. *Sci. Adv.* **9**, eadf8332 (2023).

635 34. D. Dong, *et al.*, Compressed sensorimotor-to-transmodal hierarchical organization in
636   schizophrenia. *Psychol. Med.* **53**, 771–784 (2023).

637 35. M. Xia, *et al.*, Connectome gradient dysfunction in major depression and its association with gene
638   expression profiles and treatment outcomes. *Mol. Psychiatry* **27**, 1384–1393 (2022).

639 36. S. Marek, *et al.*, Reproducible brain-wide association studies require thousands of individuals.
640   *Nature* **603**, 654–660 (2022).

641 37. T. Xu, *et al.*, ReX: an integrative tool for quantifying and optimizing measurement reliability for the
642   study of individual differences. *Nat. Methods* **20**, 1025–1028 (2023).

643 38. H. van Kippersluis, *et al.*, Overcoming attenuation bias in regressions using polygenic indices.
644   *Nat. Commun.* **14**, 4473 (2023).

645 39. J. N. Pritikin, M. C. Neale, E. C. Prom-Wormley, S. L. Clark, B. Verhulst, GW-SEM 2.0: Efficient,
646   Flexible, and Accessible Multivariate GWAS. *Behav. Genet.* **51**, 343–357 (2021).

Bignardi et al.

647 40. A. D. Grotzinger, *et al.*, Genomic structural equation modelling provides insights into the
648   multivariate genetic architecture of complex traits. *Nat. Hum. Behav.* **3**, 513–525 (2019).

649 41. M. F. Glasser, *et al.*, The minimal preprocessing pipelines for the Human Connectome Project.
650   *NeuroImage* **80**, 105–124 (2013).

651 42. B. T. T. Yeo, *et al.*, The organization of the human cerebral cortex estimated by intrinsic
652   functional connectivity. *J. Neurophysiol.* **106**, 1125–65 (2011).

653 43. E. W. Dijkstra, A note on two problems in connexion with graphs. *Numer. Math.* **1**, 269–271
654   (1959).

655 44. R. Vos de Wael, *et al.*, BrainSpace: a toolbox for the analysis of macroscale gradients in
656   neuroimaging and connectomics datasets. *Commun. Biol.* **3**, 1–10 (2020).

657 45. R. A. I. Bethlehem, *et al.*, Dispersion of functional gradients across the adult lifespan.
658   *NeuroImage* **222**, 117299 (2020).

659 46. T. K. Koo, M. Y. Li, A Guideline of Selecting and Reporting Intraclass Correlation Coefficients for
660   Reliability Research. *J. Chiropr. Med.* **15**, 155–163 (2016).

661 47. Y. Rosseel, lavaan: An R Package for Structural Equation Modeling. *J. Stat. Softw.* **48**, 1–36
662   (2012).

663 48. T. C. Bates, H. Maes, M. C. Neale, umx: Twin and Path-Based Structural Equation Modeling in R.
664   *Twin Res. Hum. Genet. Off. J. Int. Soc. Twin Stud.* **22**, 27–41 (2019).

665 49. D. Boomsma, A. Busjahn, L. Peltonen, Classical twin studies and beyond. *Nat. Rev. Genet.* **3**,
666   872–882 (2002).

667 50. B. Verhulst, E. Prom-Wormley, M. Keller, S. Medland, M. C. Neale, Type I Error Rates and
668   Parameter Bias in Multivariate Behavioral Genetic Models. *Behav. Genet.* **49**, 99–111 (2019).

669 51. A. M. Mowinckel, D. Vidal-Piñeiro, Visualization of Brain Statistics With R Packages ggseg and
670   ggseg3d. *Adv. Methods Pract. Psychol. Sci.* **3**, 466–483 (2020).

671

672
673
674
675
676
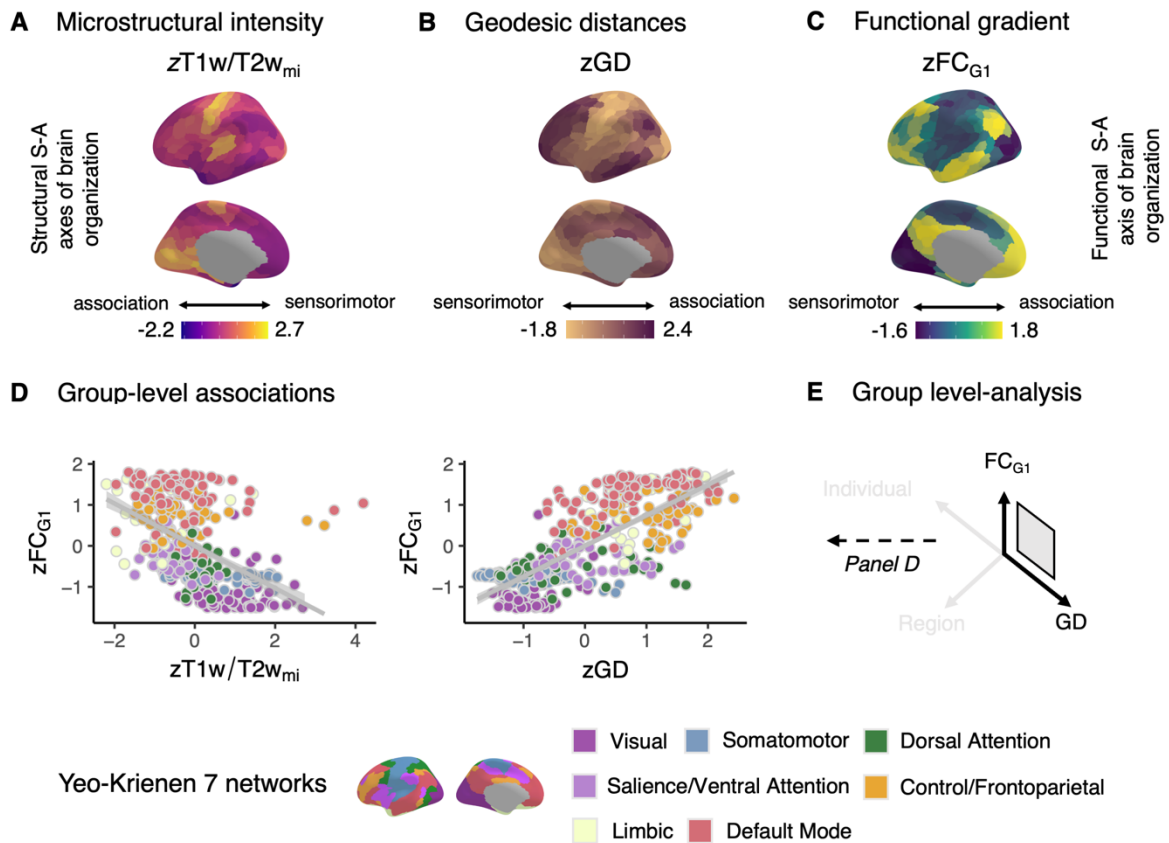677
678
679
680
681
682
683
684
685
686
687
688
689
690

Bignardi et al.

Figures

Figure 1. Structural and functional S-A axes strongly correlate at the group-level. Structural (**A-B**) and functional (**C**) indices of Sensorimotor-Association (S-A) axes plotted on inflated cortical surfaces (51). Values represent averages of individual T1w/T2w mean intensity profiles (A; T1w/T2w$_{mi}$), averages of individual Geodesic Distances (B; GD), and functional gradients loadings (C; FC$_{G1}$) extracted from the average of individual functional connectomes across 400 cortical regions. (**D**) Structural indices are strongly associated with functional indices of the S-A axis; Spearman ρ=-.61 and ρ=.75 between T1w/T2w$_{mi}$ and FC$_{G1}$, and GD and FC$_{G1}$, respectively; all $p<.05$). Each dot represents a regional value; the colour represents Yeo-Krienen 7 network membership. (**E**) Conceptual representation of group-level analysis. Note that individual and regional information is lost in favour of group-level results.

Bignardi et al.
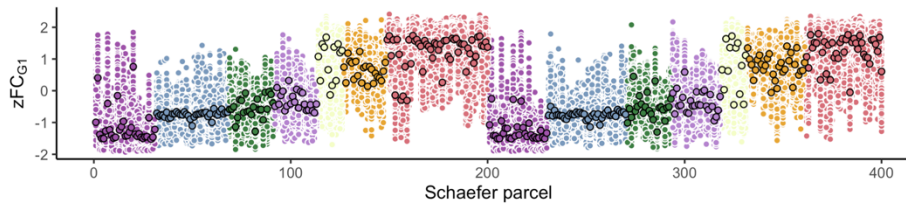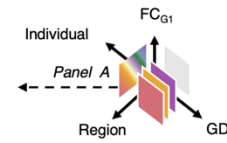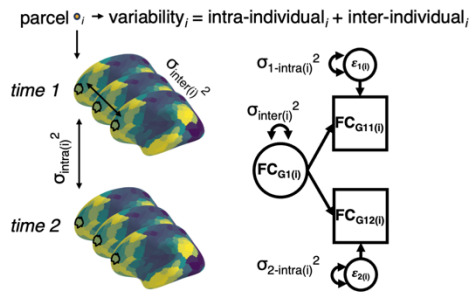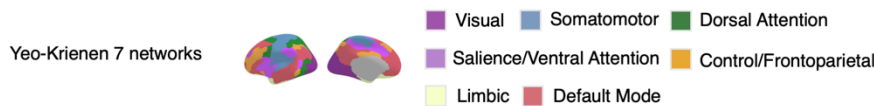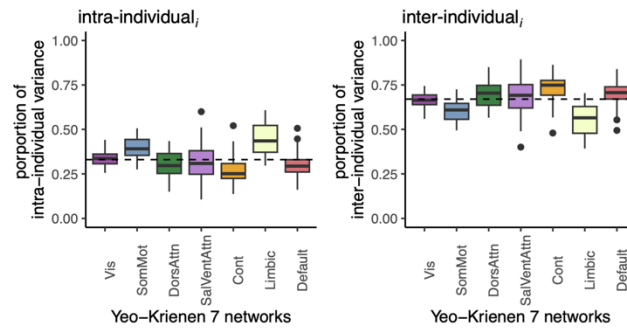
Figure 2. Pervasive inter-individual differences in the S-A axis of functional connectivity. (**A**) group-level estimates (black contour) overshadow pervasive individual differences in S-A axis properties. (**B**) The shift between levels of analyses: from group-level (grey square) to between-individuals (coloured squares); The gradient square conceptually captures panel A. (**C**) Conceptual and formal measurement error model to partition, for any parcel i, variance in the functional gradient loadings into intra- ($\sigma_{d\text{-}intra(i)}^2$, for regional values measured at day 1 or 2 of the testing session, i.e., squares) and inter- ($\sigma_{inter(i)}^2$, for the latent component, i.e., circle) individual variance. Parameter estimates for any parcel i can be found in Supporting File 1. (**D**) The proportion of intra- and inter-individual variance in the functional network across Yeo-Krienen functional networks: the horizontal line displays the median; lower and upper hinges correspond to the first and third quartile; the whisker extends from the hinge to the largest/lower value no further than 1.5 * interquartile range from the hinge. Note that across all parcels, observed variance includes substantial inter-individual variation. *Notes on measurement model: Squares represent the measured phenotypes; The circle is the latent component; the double-headed arrows within the circle represent the variance associated with the latent components; one-headed arrows are the paths (here all set to 1).*

Bignardi et al.
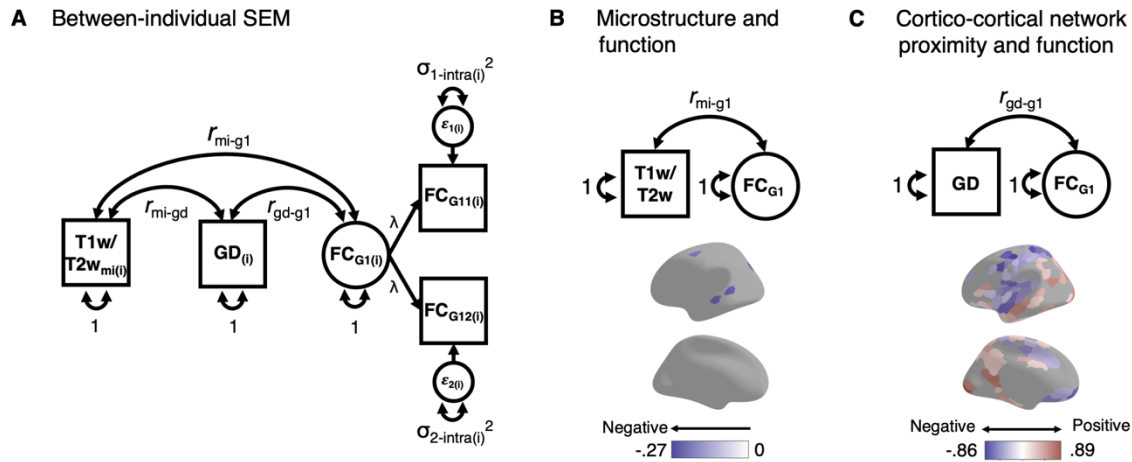
Figure 3. **Structural and functional S-A axes selectively correlate between individuals.** (**A**) Simplified structural measurement error model to estimate the correlation between S-A axis properties considering the distinction between intra- and inter-individual differences in functional gradient loading variability. Observed parcel-wise values and latent components are standardised before model fitting. (**B-C**) Summary for the standardised estimates on the inflated cortical surface (51) from the structural measurement error model indicates little and weak overlaps between microstructural intensity (T1w/T2w$_{mi}$) and functional gradient loadings (FC$_{G1}$) inter-individual differences but large and highly significant ($p<.05$ corrected for Bonferroni comparisons) overlaps between functional gradient loadings and geodesic distances (GD). All parameter estimates for any parcel i, including the covariances between T1w/T2w$_{mi}$ and GD that were not the focus of the current study, can be found in Supporting File 2. *Notes on structural equation models: double-headed arrows between circles represent covariances; here, path coefficients for the measurement error model are estimated (λ). Other abbreviations and symbols are as in Figure 2.*
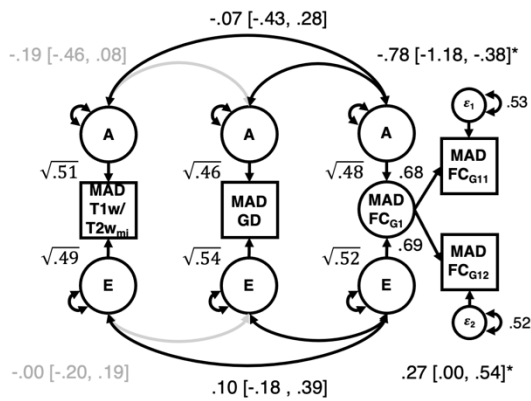
Bignardi et al.
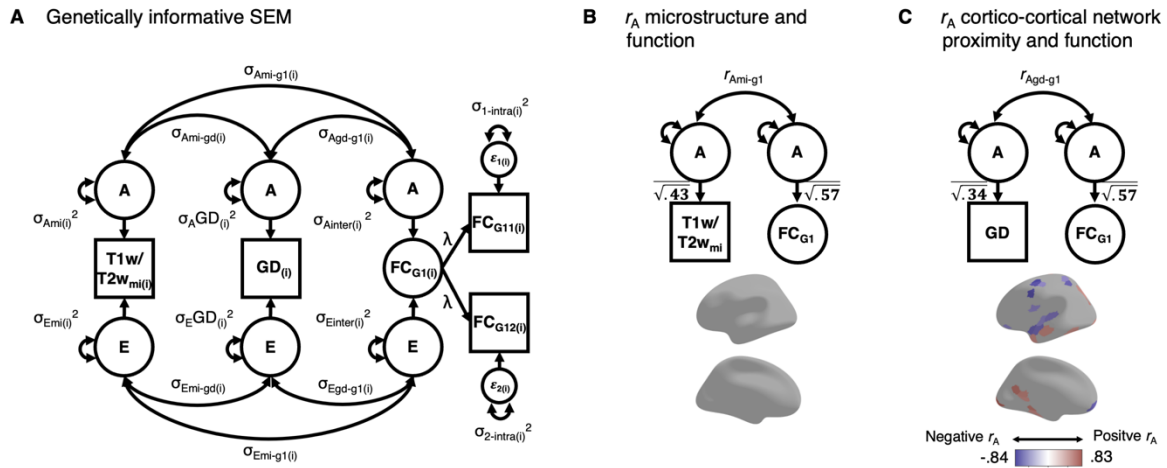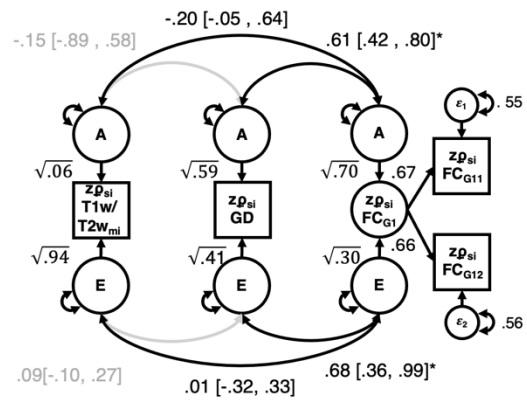

Figure 4. Genetic sources of the S-A axis' structural and functional properties are selectively distinct. (**A**) Simplified graphical representation of the multivariate twin-informed SEM. All parameter estimates for any parcel *i* can be found in Supporting File 3. (**B-C**) simplified summary for the significant additive genetic correlations (r_A) across S-A axis properties on the inflated cortical surface (46) indicates only significant genetic correlations between cortico-cortical network proximity, as measured by geodesic distances (GD) and functional gradients loadings (FC$_{G1}$). Note that since we report here (average) standardised path coefficient estimates, the double-headed arrow between the two additive genetic components can now be interpreted as r_A. r_A estimates can be found in Supporting Files 4-5 (B-C, respectively). *Notes on structural equation models: additional circles represent latent additive genetic and environmental components; Double-headed arrows between circles represent genetic and environmental covariances. Where not noted, path coefficients are set to 1. Other abbreviations and symbols are as in Figure 2.*

Figure 5. Findings extend beyond regional S-A axis associations. (A) Simplified graphical representation of the multivariate twin-informed SEM for overall within-individual Median Absolute Deviations (MAD). Note the strong but negative significant associations between the latent additive genetic components underlying geodesic distances (GD; centre) and functional gradient loadings (FC$_{G1}$; right). **(B)** Simplified graphical representation of the multivariate twin-informed SEM for ρ similarity indices (Fisher-z transformed). As for the model reported in panel A, the only significant associations are found between GD and FC$_{G1}$. * $p < .05$. *Notes on structural equation models: abbreviations and symbols are as in Fig. 4. Here, double-headed arrows between latent variables indicate correlations (since we report standardised solutions).*